Experiments in Fluids (2023) 64:181
https://doi.org/10.1007/s00348-023-03719-3

RESEARCH ARTICLE

# Image analysis techniques for in vivo quantification of cerebrospinal fluid flow

**Daehyun Kim[1] · Yiming Gan[2] · Maiken Nedergaard[3] · Douglas H. Kelley[2] · Jeffrey Tithof[1]**

Received: 21 July 2023 / Accepted: 30 September 2023


## Abstract

Over the past decade, there has been a tremendously increased interest in understanding the neurophysiology of cerebrospinal fluid (CSF) flow, which plays a crucial role in clearing metabolic waste from the brain. This growing interest was largely initiated by two significant discoveries: the glymphatic system (a pathway for solute exchange between interstitial fluid deep within the brain and the CSF surrounding the brain) and meningeal lymphatic vessels (lymphatic vessels in the layer of tissue surrounding the brain that drains CSF). These two CSF systems work in unison, and their disruption has been implicated in several neurological disorders including Alzheimer's disease, stroke, and traumatic brain injury. Here, we present experimental techniques for *in vivo* quantification of CSF flow via direct imaging of fluorescent microspheres injected into the CSF. We discuss detailed image processing methods, including registration and masking of stagnant particles, to improve the quality of measurements. We provide guidance for quantifying CSF flow through particle tracking and offer tips for optimizing the process. Additionally, we describe techniques for measuring changes in arterial diameter, which is an hypothesized CSF pumping mechanism. Finally, we outline how these same techniques can be applied to cervical lymphatic vessels, which collect fluid downstream from meningeal lymphatic vessels. We anticipate that these fluid mechanical techniques will prove valuable for future quantitative studies aimed at understanding mechanisms of CSF transport and disruption, as well as for other complex biophysical systems.

## 1 Introduction

Cerebrospinal fluid (CSF) envelops the brain and spinal cord, acting as a cushion that provides buoyancy (Wright et al. 2012) and supplying nutrients (Wright et al. 2012; Spector et al. 2015). Growing evidence suggests that CSF also plays an important role in metabolic waste removal (Abbott 2004; Iliff et al. 2012; Spector et al. 2015; Hablitz and Nedergaard 2021). Since the brain parenchyma is devoid of lymphatic vessels, researchers have speculated for decades that CSF circulation may serve a pseudo-lymphatic role (Milhorat 1975). Tracer injection experiments from the past decades (Cserr and Ostrach 1974; Cserr et al. 1981; Rennels et al. 1985) demonstrated that solute exchange between the CSF and interstitial fluid (ISF) occurs at rates faster than diffusion alone, indicating the presence of bulk flow through perivascular spaces (PVSs), which are annular channels surrounding vasculature throughout the brain. Several high-profile discoveries from the past decade (Iliff et al. 2012; Xie et al. 2013; Louveau et al. 2016; Mestre et al. 2018; Mesquita et al. 2018; Ahn et al. 2019; Mestre et al. 2020; Møllgård et al. 2023) have inspired growing interest in CSF research due to their profound implications for improving health. However, many questions remain regarding the direction, key compartments, and mechanisms of CSF flow throughout the central nervous system.

The precise details of solute exchange between CSF and ISF are not well-established, with multiple competing hypotheses in the literature. The intramural periarterial drainage (IPAD) hypothesis posits that basement membranes (i.e., vessel walls) of cerebral capillaries and arteries are the main efflux route by which ISF exits the brain (Weller 1998;

✉ Jeffrey Tithof
tithof@umn.edu

[1] Department of Mechanical Engineering, University of Minnesota, 111 Church St SE, Minneapolis, MN 55455, United States

[2] Department of Mechanical Engineering, University of Rochester, Hopeman Engineering Bldg, Rochester, NY 14627, United States

[3] Center for Translational Neuromedicine, University of Rochester Medical Center, 601 Elmwood Ave, Rochester, NY 14642, United States

Published online: 30 October 2023

Albargothy et al. 2018; Aldea et al. 2019). This hypothesis is largely motivated by observations of amyloid-$\beta$ (a protein waste molecule linked to neurodegenerative diseases) aggregation on arteries, which is a hallmark feature of cerebral amyloid angiopathy (Yamada 2015). Carare et al. (2008) reported that soluble tracers diffuse through the brain parenchyma and then drain through basement membranes, indicating that ISF is transported retrograde to blood flow. However, it is important to note that the vast majority of experimental evidence supporting the IPAD hypothesis is derived from ex vivo analysis of fixed tissue, which is subject to anatomical changes and irregular flows that occur during the fixation process (Mestre et al. 2018). Alternatively, the glymphatic (glial-lymphatic) hypothesis suggests that CSF follows a pathway that is anterograde to blood flow, flowing inward along PVSs of arteries, continuing through the brain interstitium, then exiting via venous PVSs (Iliff et al. 2012; Jessen et al. 2015; Mestre et al. 2017). Within the framework of either hypothesis, arterial pulsations are widely acknowledged as a likely mechanism driving bulk CSF/ISF flow (Hadaczek 2006; Schley et al. 2006; Iliff et al. 2012; Mestre et al. 2018). Several prior studies have analytically and numerically modeled arterial pulsations to investigate the feasibility of this driving mechanism (Wang and Olbricht 2011; Diem et al. 2017; Asgari et al. 2016; Rey and Sarntinoranont 2018), which has led to a third hypothesis: that arterial pulsations generate oscillatory (net zero) flow that enhances transport via Taylor dispersion (Asgari et al. 2016). We point the reader to several review articles for a more extensive discussion of CSF/ISF transport hypotheses (Ray and Heys 2019; Rasmussen et al. 2021; Agarwal and Carare 2021; Hladky and Barrand 2022; Kelley and Thomas 2022; Bohr et al. 2022).

CSF drains from the skull through multiple parallel efflux routes including along cranial nerves that penetrate the cribriform plate (Norwood et al. 2019; Decker et al. 2022; Ma et al. 2017; Spera et al. 2023), through basal and dorsal meningeal lymphatic vessels (Louveau et al. 2015; Aspelund et al. 2015), to the spinal canal (Murtha et al. 2014), and directly into the blood at the superior sagittal sinus (Møllgård et al. 2023); however, the exact contribution of each route is not well understood (Proulx 2021). Further complicating the matter, recent research suggests that the rate and distribution of CSF production and outflow varies depending on the circadian rhythm (Steffensen et al. 2023; Hablitz et al. 2020). Regardless of the exact details of outflow dynamics, it has long been appreciated that a substantial portion of CSF drainage eventually reaches cervical lymphatic vessels located in the neck (Bradbury and Cole 1980; Arnold et al. 1973), and the discovery of meningeal lymphatic vessels supports the idea that the lymphatic system constitutes a significant CSF outflow route. Ultimately, many open questions remain due to experimental challenges and technical limitations associated with probing small length scales deep inside or adjacent to the skull.

Numerous experimental approaches exist for measuring CSF flow (Bohr et al. 2022), but each has different benefits and drawbacks. In this article, we describe image analysis techniques for quantifying CSF flow, applied to time series of two-dimensional (2D) images that were recorded using two-photon microscopy (TPM). TPM offers excellent spatial and temporal resolution (as high as about 0.5 µm/pixel at 60 Hz), enabling detailed fluid mechanical analysis of CSF dynamics through PVSs at the surface of the brain (Mestre et al. 2018, 2020; Raghunandan et al. 2021; Hussain et al. 2023) or through cervical lymphatic vessels in the neck (Hussain et al. 2023; Du et al. 2023). An important appealing feature of TPM is that it relies on *two-photon* fluorophore excitation which depends quadratically on the incident photon flux, and thus by focusing a laser at a precise location, fluorescence is achieved in a tiny volume of approximately 1 $\mu m^3$ (So et al. 2000). By rastering pixel-by-pixel throughout a plane, 2D images are achieved at a precise depth with negligible fluorophore excition above/below that plane; this is in contrast with other microscopy techniques (e.g., confocal). In 2018, Mestre et al. (Mestre et al. 2018) leveraged TPM to demonstrate that CSF flows parallel (not anti-parallel) to blood through approximately 40 µm wide PVSs at the surface of the brain, and the flow pulses in synchrony with the cardiac cycle (Mestre et al. 2018) (anesthetized mice have a heart rate on the order of 5 Hz, so a Nyquist rate $\gtrsim$ 10 Hz is needed to resolve the flow pulsatility). Subsequently, these techniques were further refined and utilized to quantify changes in CSF dynamics following stroke (Mestre et al. 2020), cardiac arrest (Du et al. 2021), and traumatic brain injury (Hussain et al. 2023). We posit that as research interest in CSF flow continues to grow due to its increasingly apparent relevance to a variety of chronic and acute neurological conditions (Rasmussen et al. 2018; Nedergaard and Goldman 2020), *in vivo* optical measurement techniques in animal models will continue to provide valuable insight into CSF dynamics. However, it is important to note the limitations of TPM: This technique requires invasive surgery to place a cranial window enabling optical access to the brain, the field of view is limited, and imaging is restricted to the top few hundred µm of the cortex since brain tissue scatters light. Insights from high-resolution measurements, obtained using techniques such as those described in this article, will likely prove most valuable when integrated into a comprehensive framework that includes other modalities for measuring CSF transport, such as magnetic resonance imaging (MRI) (Battal et al. 2011; Bradley 2015; Eide et al. 2018; Ringstad et al. 2018), transcranial brain-wide epifluorescence microscopy (Plog et al. 2018; Sweeney et al. 2019), and *ex vivo* tissue fixation with histological staining (Cserr and Ostrach 1974; Cserr et al.

1981; Rennels et al. 1985; Weller 1998; Albargothy et al. 2018; Aldea et al. 2019; Carare et al. 2008). For a more comprehensive discussion of various measurement techniques, we point the reader to Bohr et al. (2022).

In this article, we provide an overview of image analysis techniques that enable quantitative characterization of CSF dynamics. Our MATLAB-based scripts, along with a short time series of images and a concise working example, are freely available online (Kim et al. 2023). A key component of the analysis involves particle tracking velocimetry (PTV), which has been used extensively for quantifying biological phenomena including respiratory flows (Jonas et al. 2011; Wang et al. 2020; Li et al. 2022), cell migration (Hilsenbeck et al. 2016; Manzo and Garcia-Parajo 2015; Salminen et al. 2020), and blood flow (Vennemann et al. 2007; Sengupta et al. 2012; Gülan et al. 2012). We perform PTV and not particle image velocimetry (PIV) because the latter requires high particle densities that may rapidly clog drainage pathways and alter CSF flow; furthermore, high particle densities would likely exacerbate particle aggregation in the PVSs (a challenge discussed in detail below). We do not provide any discussion of surgical techniques required prior to imaging CSF flow *in vivo*; rather, we direct the reader to references (Sweeney et al. 2019; Xavier et al. 2018).

This article is structured as follows. First, Sect. 2 provides a brief overview of experimental methods and image analysis techniques described in this article. We then discuss image preprocessing in Sect. 3, including image registration and masking stagnant microspheres, which both improve the reliability of CSF flow measurements. We provide insight and recommendations for choosing near-optimal tracking parameters in Sect. 4. Then, we introduce techniques for quantifying changes in vessel diameter, which are thought to contribute to CSF transport, in Sect. 5. Next, we demonstrate in Sect. 6 how the aforementioned techniques can be adapted and applied to measure fluid flow through cervical lymphatic vessels. Finally, a summary and conclusions are provided in Sect. 7. An appendix is also included (section A) which presents an uncertainty analysis of PTV based on TPM imaging.

## 2 Overview of experimental methods

The image analysis techniques presented in this article require injection of fluorescent tracers to visualize different fluid compartments in the brain. To enable quantitative measurement of CSF flow via PTV, fluorescent microspheres (FluoSpheres, diameter 1.0 µm) were injected into the CSF, which is usually performed at the cisterna magna (an accessible region near the posterior skull base) (Mestre et al. 2018; Xavier et al. 2018; Ramos et al. 2019). Note that the number of particles that appear in PVSs is highly variable (see Supplementary Table 1 in ref. Mestre et al. (2018)), so long time series ($\gtrsim$ 20 min) are desirable to obtain a reliable estimate of the CSF flow velocity in cases of few particles. Although some researchers have raised concerns that invasive tracer injections increase the intracranial pressure and may result in non-physiological flow (Smith and Verkman 2018; Croci et al. 2019; Vindedal et al. 2016; Faghih and Sharp 2021; Vinje et al. 2020), Raghunandan et al. (2021) demonstrated that flow velocities in PVSs are unchanged (compared to prior experimental protocols) when injections are performed using a dual syringe that injects and withdraws fluid, minimally disrupting the intracranial pressure. Fluorescent microspheres in the CSF appear as green dots in Fig. 1a. Experiments typically also include injection of fluorescent dye into the blood for visualization, which may be an intravenous or retro-orbital injection (Yardeni et al. 2011). Visualizing the blood compartment is valuable for inferring the approximate location of the PVS (by definition, PVSs are adjacent to blood vessels and the vascular wall forms the inner boundary of each PVS). Such visualization also facilitates image registration and enables measurement of arterial pulsations, both described below. We note that here, as well as in prior publications (Mestre et al. 2018, 2020; Du et al. 2021), the color channels for CSF microspheres (green) and blood (red) have been swapped from their true fluorescence (red and green, respectively) to facilitate an intuitive representation of blood with the color red.

After a time series of microspheres flowing through the PVSs is recorded, we perform Lagrangian particle tracking using a predictive algorithm (Ouellette et al. 2006; Kelley and Ouellette 2011). For a given snapshot (e.g., Fig. 1a), particles are first detected based on a pixel intensity threshold, and the centroid is identified for each contiguous region above that threshold. Identified particles are then linked in time by matching a given centroid to a nearby centroid in the next frame using kinematic predictions. The maximum search radius for linking sequential centroids in time is user-specified and should be chosen carefully (see below). Once particle tracking is completed, we plot the superimposed tracks from the entire time-series recording, which provides a visual assessment of the PVS size and shape (Fig. 1b). PVS size/shape can also be characterized through infusion of fluorescent dyes (e.g., dextran and bovine serum albumin) into the CSF (Iliff et al. 2012, 2013; Mestre et al. 2018), but these small molecules can cross from the PVS into the brain interstitium, potentially obscuring interpretation of the location of the PVS outer boundary (which is formed by astrocyte endfeet). Finally, velocity measurements from the entire time series are spatially binned and averaged to obtain the mean CSF velocity (Fig. 1c), and the magnitude of each vector provides the flow speed (Fig. 1d). Note that an inherent limitation is that these measurements are 2D. To improve the accuracy and reliability of the resulting velocity

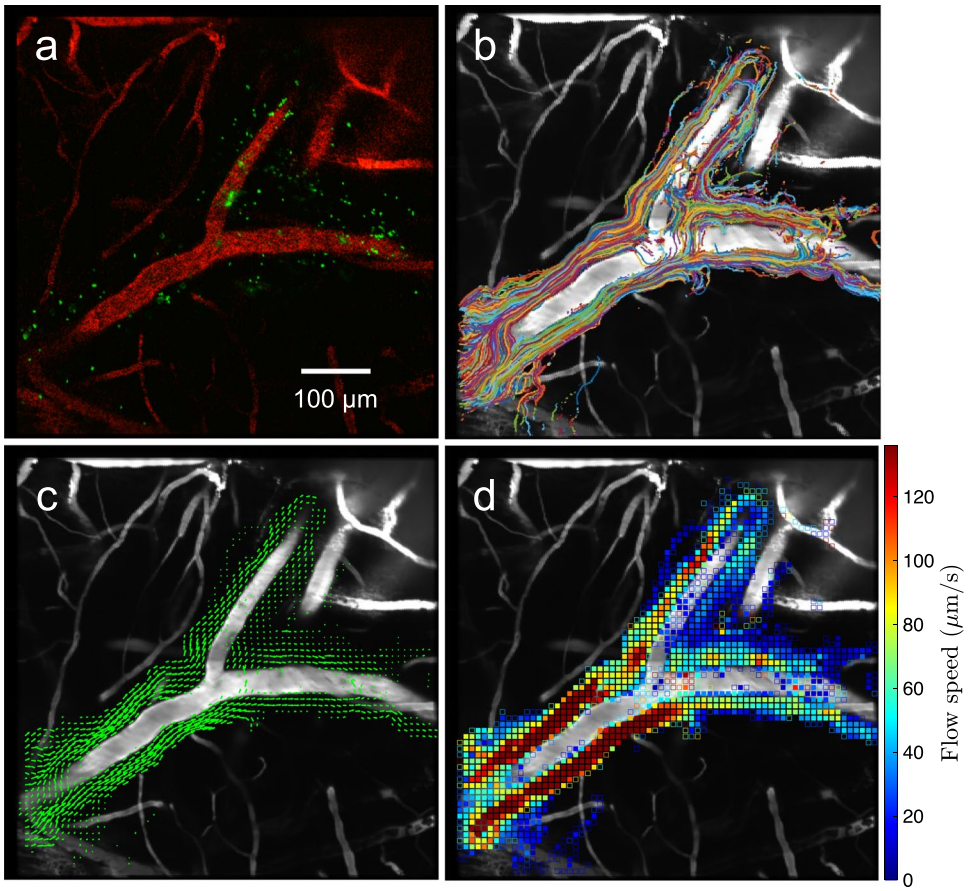


**Fig. 1** An example of image analysis to quantify CSF flow through PVSs at the surface of a mouse brain. Fluorescent tracers are injected into the blood (bovine serum albumin) and CSF (1 μm polystyrene microspheres) and then recorded *in vivo* using two-photon microscopy by imaging through a cranial window. **a** A snapshot of a pial artery (red) and fluorescent microspheres (green) acquired at 30 Hz. **b** Superimposed trajectories of the microspheres obtained from PTV, which can be used to visualize the size of the PVSs. **c-d** Time-averaged (**c**) 2D velocity field and (**d**) flow speed (i.e., magnitude of the velocity field) quantifying the net CSF transport

measurements, we perform image preprocessing, including image registration and masking of stagnant microspheres; these two procedures are presented in the next section.

## 3 Image preprocessing

As described in the previous section, we obtain measurements of net CSF velocity in PVSs at the surface of the brain by performing *in vivo* PTV followed by spatial binning and averaging of all measurements. Since these measurements are performed *in vivo*, some amount of relative motion between the microscope and the living mouse is practically unavoidable. Our recordings are necessarily obtained in the fixed reference frame of the microscope and hence should be transformed to a fixed reference frame of the region of the brain under consideration. We perform this transformation via image registration, which is described next in Sect. 3.1. Afterward, in Sect. 3.2, we discuss issues of microsphere aggregation and adherence to PVS boundaries, then present methods for masking these stagnant particles. Both image registration and masking techniques have been applied in prior studies (Diezmann et al. 2017; Hill et al. 2001; Hand et al. 2009; Ergin 2017; Charogiannis et al. 2015) to improve accuracy of particle tracking and/or particle image velocimetry.

### 3.1 Registration

A significant challenge faced when performing *in vivo* CSF imaging is that the field of view may translate, which may occur in the $x-y$ plane or perpendicular to it (along $z$), over short or long time scales. These shifts may be attributed to: (i) cardiac/respiratory cycles (short time scales), (ii) thermal expansion of imaging components (long), and/or (iii) small amounts of brain swelling resulting from cranial window placement (long). Five snapshots from an imaging time series are shown in Fig. 2a, for which subtle, long time scale translations occurred during the recording. This shift is perhaps most apparent from features in the top left corner, where some vessels are out of the field of view at $t = 0$, but become visible at $t = 337$ s. This appearance of a new vascular structure near the boundary is indicative of a shift in the $x-y$ plane. Additionally, there is an X-shaped configuration of vessels near the bottom left corner which is most apparent at times $t = 337$ and 1350 s. Appearance/disappearance of vasculature away from the boundaries is indicative of a shift in the imaging

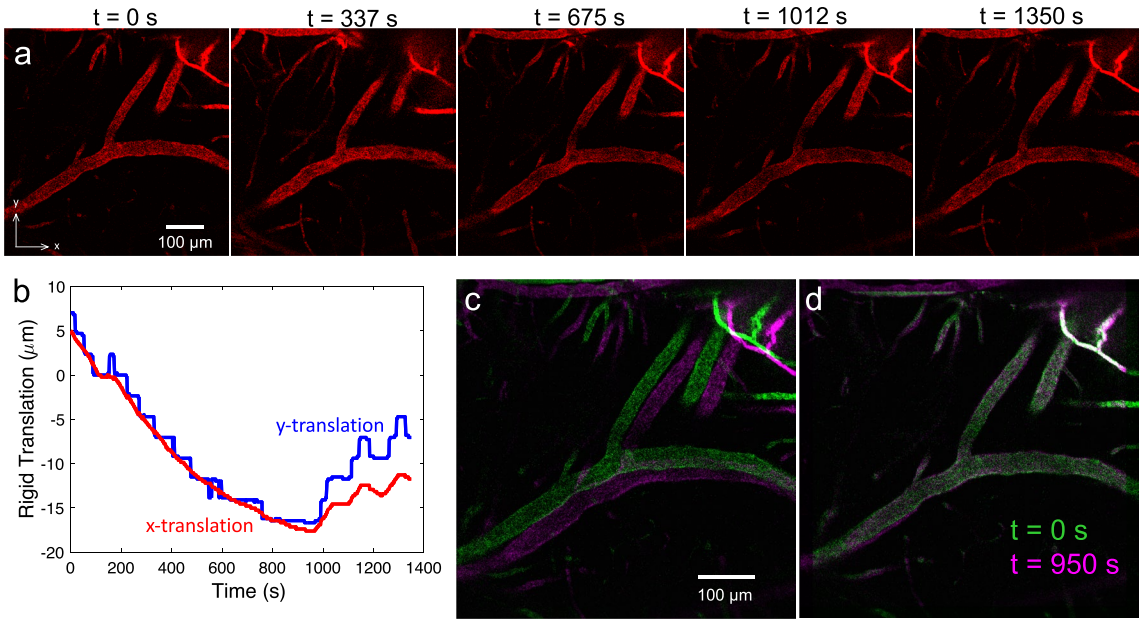


**Fig. 2** Example illustrating image registration in the vicinity of a pial artery. **a** Snapshots from a time series which show a small, gradual translation in the field of view. **b** Plot of the $x$-directional and $y$-directional translations that occur in time series, computed via cross-correlation with a reference frame; these translations are used for image registration. **c–d** Comparison of images at $t = 0$ s (green) and $t = 950$ s (magenta) (**c**) before and (**d**) after registration is performed

plane along the $z$-direction (recall that for TPM, images are acquired at a precise plane with depth of about 1 μm). There are limited means for accounting for a shift along $z$. Translations of the field of view, if not corrected for, will result in erroneous velocity measurements for two reasons: (i) Motion of a particle between sequential frames will be due to both fluid flow and imaging plane translation, and (ii) PVSs will appear wider with blunted time-averaged peak flow speeds.

To register images, we perform a spatial cross-correlation between a reference snapshot and every other snapshot in the time series to determine the transformation necessary to shift each image in the time series to a common reference frame. For flow through PVSs, we have found that registration that only accounts for rigid translation is adequate (i.e., rotation and deformation are unnecessary). We choose the reference snapshot typically as a frame (or time-average a short segment of frames to reduce noise) from a relatively stable instant in the recording, which we identify by visually inspecting a sped up animation of the TPM time series. After obtaining the cross-correlation peak for each frame, all frames in all channels are registered to the reference frame by applying a rigid translation (Fig. 2b). We note that it is necessary to increase the dimensions of the registered images by a number of pixels equal to the absolute value of the difference in maximum and minimum translations along each direction (e.g., based on Fig. 2b, approximately $4 - (-15) = 19$ pixels must be added). This is so that the original image may be translated within the bounds of the registered image domain.

A successful application of image registration is illustrated in Fig. 2c-d wherein two snapshots of a pial artery are superimposed with different colors indicating time: green at $t = 0$ s and magenta at $t = 950$ s. Figure 2c shows these snapshots prior to registration, where there is a clear offset in the position of the vasculature; in Fig. 2d, which shows the post-registration snapshots, the colocalization of green and magenta indicates that the alignment is excellent. This figure also conveys details of the translation that occurred during imaging: Near the top left of Fig. 2d, a segment of vasculature is purely magenta with no green, indicating that segment became visible at later times ($t = 950$ s) as the field of view translated in the positive $y$-direction.

## 3.2 Masking

As the fluorescent microspheres advect with the CSF flow, some of these particles adhere to the boundaries of the PVS. Once this occurs, they rarely become unstuck. In general, the reasons for particle aggregation and adherence to tissue are not well understood, but may be due to surface charge interactions or regions with fibrous obstructions forming a mesh that particles become trapped in (e.g., stomata that enable CSF exchange between pial PVSs and the subarachnoid space Abbott et al. 2018). Figure 3a shows a snapshot with an inset that provides an enlarged view of a region with

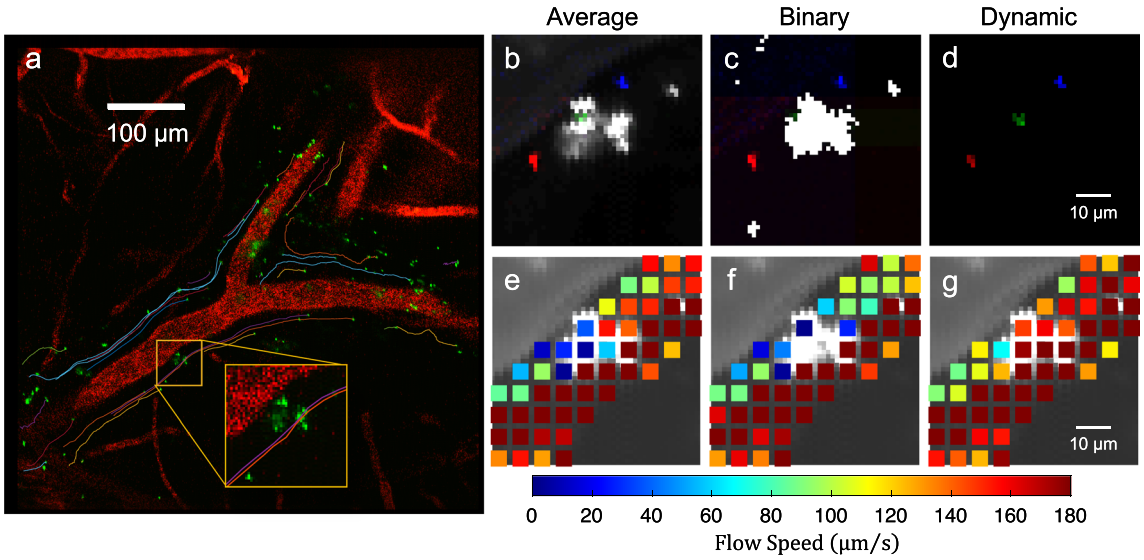


**Fig. 3** Comparison of masking methods. **a** Image of a pial artery with colored curves indicating the tracking of fluorescent microspheres flowing in the adjacent PVSs. No background has been subtracted for this image. (Inset) A zoomed-in image of a region containing a stagnant microsphere aggregate, which may lead to erroneous measurements of zero velocity if not properly masked. **b–d** Plots characterizing three different masking techniques (average, binary, and dynamic masking), with the mask superimposed in white/gray. Three sequential unmasked images are also superimposed in red, green, and blue indicating the trajectory of a flowing particle. **e–g** Net flow speed (i.e., the magnitude of the time-averaged velocity) obtained from particle tracking for a long time series with the indicated masking technique applied. **e** Average masking incompletely masks the region with stuck particles, leading to erroneous low-velocity measurements. **f** Binary masking completely removes measurements from the portion of the domain with stuck particles. **g** Dynamic masking leads to the best results with large velocities near the center of the channel, as expected, and no measurement voids, as in **f**

a cluster of stuck particles (yellow box). Stagnant particles may interfere with measurement of CSF flow velocity by generating erroneous zero-velocity measurements. Hence, masking the stuck region will improve the measurement accuracy.

A variety of masking approaches have been implemented in velocity measurement applications (Ergin 2017). One common masking approach is to create a “background image" by time-averaging an entire time series, then that background image is subtracted from all frames in the time series, enabling isolation of only the moving components. Figure 3b shows the time-averaged background image for the inset shown in Fig. 3a, where the pixel intensity of the background image varies from 0 to 255 (i.e., the grayscale background image has black, gray, and white values). The white regions of the image correspond to particles that stagnated early in the imaging times series, whereas gray regions correspond to regions where particle stagnation occurred later. For comparison, three sequential background-subtracted images are superimposed in red, green, and blue, indicating the time evolution of a free-flowing particle that does not adhere to the stagnant cluster. This figure illustrates that masking with a standard time-average background image may or may not obscure a free-flowing particle. Detrimentally, late in the time series when the particle aggregate becomes large, the background image intensity may not be great enough to mask the entire stagnant aggregate, leading to zero-velocity measurements. Such measurements are erroneous, as particles are still clearly flowing through the PVS at a slightly different depths from the stagnant aggregate.

A second masking approach is to replace the time-averaged background image with a binary background image. The purpose of generating a binary background image is to completely mask any region with stagnant particles. Figure 3c shows the background image obtained when a low pixel intensity threshold is used to binarize the background image presented above (i.e., values above or below the threshold become 255 or 0, respectively). Again, three sequential background-subtracted images are superimposed in red, green, and blue, but the green particle is not visible, indicating that this free-flowing particle is indeed removed by this mask. However, at late times, this approach will satisfactorily mask regions with stagnant aggregates, avoiding erroneous zero-velocity measurements. Note that this approach was used in Mestre et al. (2018) and explains why Figs. 1d and 5a in that manuscript have interspersed voids in the flow speed heatmap plots.

A third and final approach is dynamic masking whereby a separate background image is generated and subtracted from each image in the time series based on the average of the closest $n$ frames in time, where $n$ is user-specified (usually corresponding to about 5 s). In this approach, at any given

frame, the spatial region that is masked will have a size and intensity that is much closer to optimal for masking the stagnant region. Hence, stagnant particles are masked, and flowing particles are visible (Fig. 3d). This often even allows for tracking of particles that pass directly over/under a stagnant region, wherein the flowing particle transiently increases the local image intensity. The superiority of dynamic background masking is readily apparent when comparing Fig. 3e-g, where average masking yields reduced flow speeds near the center of the channel (Fig. 3e), binary masking yields measurement voids near the center of the channel (Fig. 3f), and dynamic masking yields reasonable, large velocities near the center of the channel (Fig. 3g). Note that dynamic masking was used for all particle tracking results presented in Mestre et al. (2020), Du et al. (2021), Holstein-Rønsbo et al. (2023), and Hussain et al. (2023).

## 4 Particle tracking parameter selection

In this section, we introduce some best practices and provide general guidelines for optimizing input parameters for PTV. The goal of PTV is to obtain reliable estimates of fluid flow velocity which generally become increasingly accurate as more measurements are added. Hence, it is ideal to maximize the total number of (reliable) measurements, which can be achieved by increasing the number of particles that are tracked and/or by increasing the number of frames over which a given particle is tracked. Here, we discuss three important parameters that affect the efficacy of PTV: threshold, minimum area, and maximum displacement (these three quantities are defined in Table 1). Figure 4a shows in blue how the mean particle track length (i.e., the average number of measurements per tracked particle) and in orange how the total number of tracks vary with each of these three parameters. Note that in all three cases, the “mean length" curve is non-monotonic with a peak, indicating that an optimal parameter value exists that maximizes the mean length of the tracks. These peaks help guide the choice of the approximate optimal parameters, which is explained in more detail in the following paragraphs. An uncertainty analysis of PTV is presented in Appendix A.

As mentioned above, the threshold sets a minimum pixel intensity value for identifying a particle. The two-photon microscopy images we analyze are 16-bit, meaning that the pixel intensity values vary from 0 to 65,535, so the threshold should also be chosen in this range. The choice of a high threshold (purple in Fig. 4b-c) will lead to smaller identified particles (since fewer pixels are above that given threshold). Conversely, the choice of a lower threshold (yellow in Fig. 4b-c) will lead to larger particles, but too low of a threshold (orange in Fig. 4b-c) will lead to erroneous identification of many particles if that threshold approaches the noise floor of the images (orange specks in the bottom of Fig. 4b and green spikes in Fig. 4c). Indeed, this effect is responsible for the large number of tracks at low threshold in Fig. 4a (top). Thus, the choice of approximate optimal parameters is more nuanced than simply maximizing the total number of measurements (equal to the mean length × number of tracks), which would occur for minimal threshold. By maximizing the mean track length, PTV typically achieves the greatest fidelity since the Lagrangian trajectories of particles will often pass through regions with different flow speeds—long tracks suggest that certain regions are not being systematically under-sampled.

The choice of minimum particle area (“Min Area" in Fig. 4a middle) is closely tied to the threshold intensity. This parameter specifies the minimum number of contiguous pixels (adjacent and diagonally connected) that must be above the chosen intensity threshold to identify and track a given particle. Consequently, as visualized in Fig. 4b-c, smaller values of the minimum area should be chosen when higher intensity thresholds are used; similarly, larger values of minimum area can be used when the intensity threshold is low, and this choice may help reduce erroneous particle identification when the threshold begins to approach the noise floor (e.g., for a threshold of 500 in Fig. 4b, which corresponds to orange, a minimum area of six would lead to identification of only three particles—the true particle in the center and two erroneous ones). In general, the choice of threshold and minimum area should be made together and may vary across different experiments depending on the fluorescent particle size, spatial resolution, and magnification.

The third parameter considered here is the maximum displacement (“Max Disp" in Fig. 4a bottom). As mentioned

**Table 1** Definition, tested range, and optimal range for particle tracking parameters from one example data set (Fig. 4)

| Parameter | Definition | Tested range (optimal range) |
|---|---|---|
| Threshold | Minimum pixel intensity value used to identify particles (16-bit images) | 500–10,000 (4000) |
| Minimum area | Minimum number of neighboring pixels (adjacent and diagonal) above threshold required to identify a particle | 1–20 (4) |
| Maximum area | Maximum allowable distance between a particle’s predicted location and actual location when tracking a particle through two sequential frames | 1 – 20 (6) |

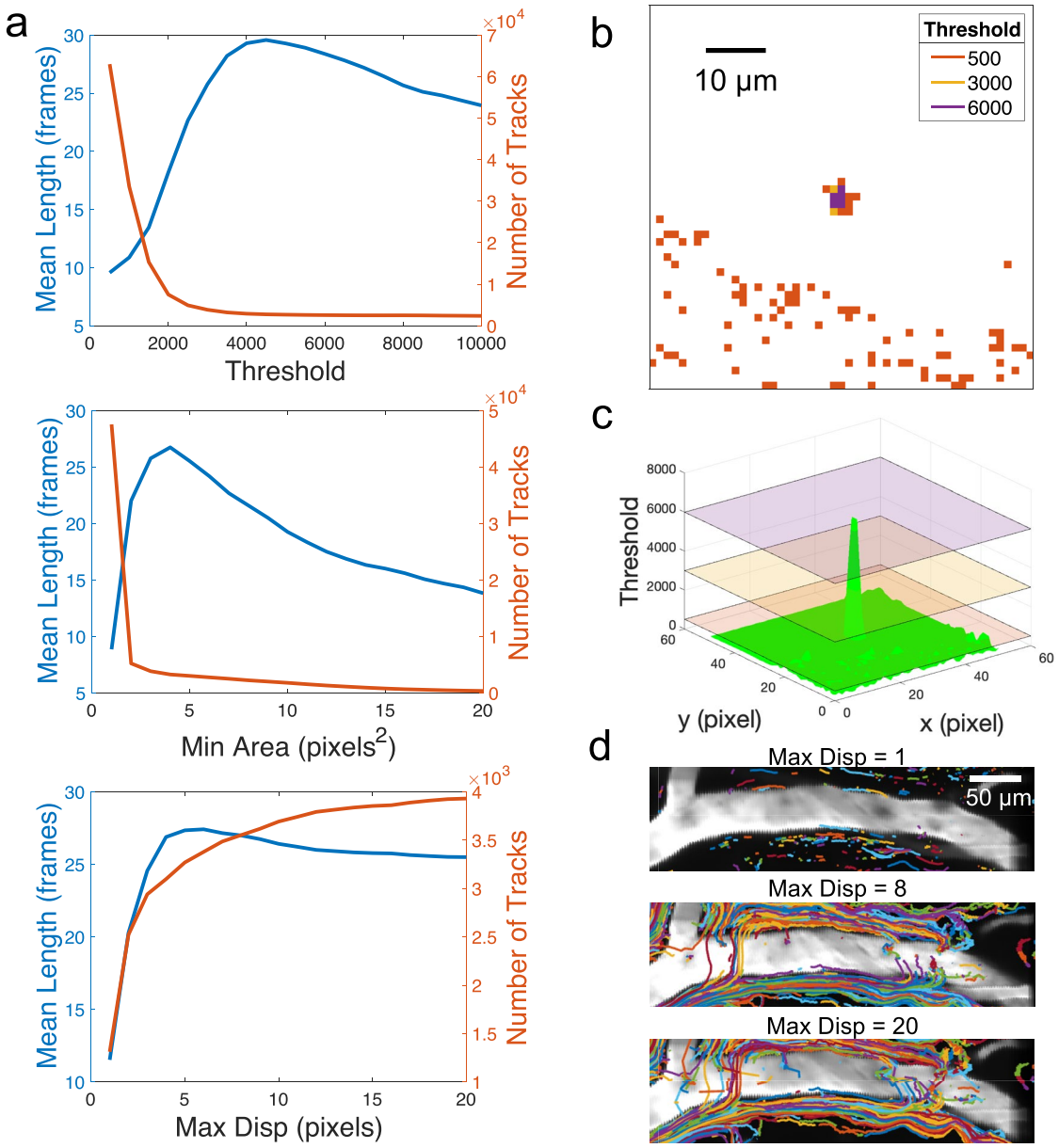


**Fig. 4** Parameter selections for PTV. **a** Plots with two *y*-axes characterizing the mean length of the particle tracks (blue) and the number of particle tracks (orange) for variations in: (top) threshold (minimum pixel intensity value used to identify particles), (middle) minimum area (minimum number of neighboring pixels above threshold required to identify a particle), and (bottom) maximum displacement (maximum allowable distance between particle's predicted and actual location when tracking). **b–c** Visualization of particle area as the pixel intensity threshold changes. Particles are identified more often and more reliably for lower threshold values, as long as the threshold is above the noise floor. **d** Higher maximum displacement increases the number of tracks, but the length of the tracks is modestly lowered. The mean track length decreases because of erroneous tracking when maximum displacement is excessively large, leading to poor kinematic predictions that result in tracking failures. This erroneous tracking appears as a sudden sharp turn in a particle trajectory and is more prevalent for a maximum displacement of 20 (bottom) than 8 (middle). For the images analyzed here, the resolution is 1.17 µm/pixel at 29.53 Hz. For tests depicted in (**a**), the variable on the *x*-axis was varied while the other two variables were fixed (threshold 3000, minimum area 3, and maximum displacement 15)

above, the particle tracking algorithm uses kinematic predictions to link and track a particle through sequential frames in time. Briefly, the maximum displacement specifies the radius over which a particle's expected position (based on a kinematic prediction, such as the average displacement over the previous few frames) can be linked to a particle identified in the next sequential frame. Note that a kinematic prediction is not available for a newly identified particle, so the maximum displacement is applied to link particles in sequential frames based on their positions (see the "Nearest Neighbor"

heuristic discussed in ref. Ouellette et al. (2006)). When the choice of the value of maximum displacement is too small, new particles cannot be linked across sequential frames because their true displacement is larger than the maximum displacement, leading to very few tracks and a small mean track length (Fig. 4a bottom; also compare Fig. 4d top and middle). As the maximum displacement is increased, the number of tracks will also increase, but as the maximum displacement becomes excessively large, the rate of erroneously linked tracks will increase (compare Fig. 4d middle and bottom). When an erroneous link occurs, it has the tendency to perturb the kinematic predictions which sometimes causes the linking to fail in sequential frames. Hence, when the maximum displacement becomes excessively large, the mean track length will decrease, as shown in Fig. 4a bottom. The ideal maximum displacement varies with spatial resolution, magnification, frame rate, and fluid velocity, so it may be difficult to predict *a priori*. Ideally imaging parameters would be chosen such that the maximum displacement is large enough to not heavily rely on subpixel identification of the particle centroid (i.e., maximum displacement $\gtrsim 3$). However, the maximum displacement should be smaller than the mean particle spacing in the image, so as to reduce the likelihood of erroneous links.

## 5 Vessel diameter measurements

The mechanism(s) driving CSF through PVSs in the brain are not yet well understood (Kelley and Thomas 2022). However, substantial evidence—both experimental (Hadaczek 2006; Iliff et al. 2013; Kiviniemi et al. 2015; Mestre et al. 2018) and theoretical (Schley et al. 2006; Wang and Olbricht 2011)—suggests that arterial pulsations arising from systolic–diastolic variations in blood pressure over the cardiac cycle contribute to CSF bulk flow via pulsations in arterial diameter. In addition to systolic–diastolic variations, recent experiments (Bojarskaite et al. 2023; Holstein-Rønsbo et al. 2023) have also demonstrated that large amplitude variations in vessel diameter occur over longer time scales due to neurovascular coupling, a process in which neuronal activity in the brain elicits arterial dilation that enhances glymphatic transport. Hence, here, we describe techniques for measuring changes in vessel diameter which can be correlated with observations of changes in CSF flow characteristics, as described in refs. Mestre et al. (2018, 2020), Du et al. (2023, 2021), and Hussain et al. (2023).

The vessel diameter measurement function we have developed requires three key user-specified inputs: The number of locations for which a vessel diameter measurement should be performed ($N$), the vessel's centerline, and the region of interest (ROI). The user first inputs $N$, then clicks two points on a representative image to specify the centerline of the vessel; finally, a region of interest is input via clicking, enabling exclusion of some regions from the analysis (e.g., adjacent vessels). Based on these inputs, the function first computes the direction perpendicular to the vessel centerline (red dashed line in Fig. 5a), then automatically computes the positions for $N$ evenly-spaced profiles to be used for automatic vessel diameter measurement throughout the time series of images (colored solid lines in Fig. 5a; $N = 5$ in this case). Anything outside of the ROI is excluded from the measurements.

To measure the vessel diameter, the pixel intensity profile of the fluorescence channel corresponding to the vasculature (red, in this case) is automatically interpolated from each 2D image to create $N$ one-dimensional profiles at each evenly-spaced location. Each pixel intensity profile is typically interpolated with higher resolution than the raw image (typically, tenfold to 100-fold). One example profile is depicted in Fig. 5b. We next identify the edges of the vessel by computing the spatial derivative of pixel intensity using a second-order accurate central finite difference (Fig. 5c). Two local maxima are then identified which we define as the edges of the vessel (red vertical lines in Fig. 5b-c). This calculation is repeated at multiple locations throughout space and in multiple frames, resulting in time series such as those shown in Fig. 5d. Such curves can be correlated with changes in CSF velocity, providing valuable insights into the underlying mechanism of CSF bulk flow in PVSs.

## 6 Extension of techniques to cervical lymphatic vessels

The image analysis techniques previously introduced can be effectively applied to cervical lymphatic vessels, which play an important role in draining CSF from the skull (Bradbury and Cole 1980; Arnold et al. 1973; Decker et al. 2022; Norwood et al. 2019; Spera et al. 2023), as discussed in the Introduction. Lymphatic vessels typically transport fluid against a mean adverse pressure difference across adjacent lymphangions (i.e., segments of lymphatic vessel separated by valves) via the combined action of contracting smooth muscle cells lining the lumen circumference and the opening/closing of bileaflet valves. This transported fluid, which includes CSF, eventually drains into the venous blood. We have recently shown that following traumatic brain injury, cervical lymphatic function becomes impaired contributing to brain edema and poor functional outcomes, but pharmacological interventions that restore lymphatic function improve functional outcomes (Hussain et al. 2023). All image analysis techniques presented above can be adapted to quantitatively measure efflux through the cervical lymphatic vessels, which we next describe.

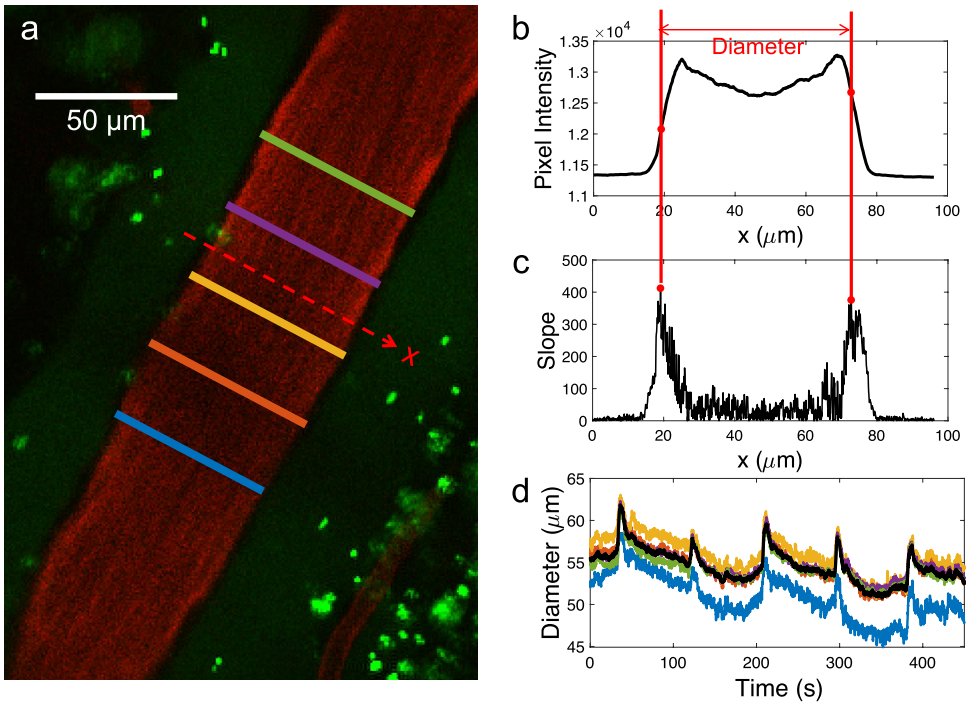


**Fig. 5** Quantitative measurements of changes in arterial diameter. **a** Two-photon microscopy image of a pial artery (red) and its adjacent PVS with several stagnant aggregated particles (green blobs). The solid colored lines indicate measurements of arterial diameter, while the dashed red line indicates an example region over which we interpolate the pixel intensity to identify the vessel diameter. **b** Plot of the interpolated pixel intensity along the red dashed line in (**a**). **c** The second-order accurate central finite difference of the pixel intensity profile in (**b**). The edges of the vessel are identified based on the two local maxima, indicated by the solid, vertical red lines. **d** Time series of the change in artery diameter with locations corresponding to the same color scheme used in panel (**a**). The solid black curve corresponds to the median across space evaluated at each instant of time. Note that the large amplitude oscillations with a period of about 9 s arise due to neurovascular coupling (alterations in local blood flow due to neuronal activity) and not cardiac pulsations

Figure 6a shows a snapshot of a TPM recording of a cervical lymphatic vessel which has been visualized using green fluorescent dye and red fluorescent microspheres. Both tracers were injected into the CSF and within about 5 min both appear in the lymphatic vessel, demonstrating that CSF directly drains via this route. The time series of images were registered using the same method described in Sect. 3.1, which is critically important. The neck region, which contains cervical lymphatic vessels and nodes, is in close proximity to the carotid arteries and respiratory tract which generate copious motion artifacts. Without registration, Fourier analysis of a velocity time series reveals substantial power associated with frequencies that coincide with the cardiac and respiratory cycles (data not shown). However, after registration, the power associated with cardiac and respiratory frequencies is greatly diminished, suggesting that image registration is crucial for obtaining accurate and reliable velocity measurements. Whereas only rigid translations were adequate for measurements in PVSs (Fig. 2), we find that including a rotational transformation significantly improves the registration quality for cervical lymphatic vessels (Fig. 6b, purple curve).

Once registration is complete, we perform particle tracking on the microspheres flowing through the cervical lymphatic vessels (red channel), enabling quantitative measurement of the spatially-averaged instantaneous flow speed (Fig. 6c). We also apply the same vessel diameter measurements introduced in Sect. 5 to the green channel to obtain measurements of the change in cervical lymphatic vessel diameter (Fig. 6d). Such diameter measurements can be used to characterize the intrinsic pumping of lymphatic vessels (Moore and Bertram 2018). Together, identifying changes in flow speed and contraction amplitude/frequency can provide crucial insights into disrupted fluid transport, as occurs following traumatic brain injury (Hussain et al. 2023).

## 7 Conclusions

Rapidly growing scientific evidence demonstrates that alterations to CSF flow through PVSs and cervical lymphatic vessels play an important role in many acute and chronic neurological conditions (Rasmussen et al. 2018; Li et al. 2022) (e.g., stroke Mestre et al. 2020, traumatic brain injury

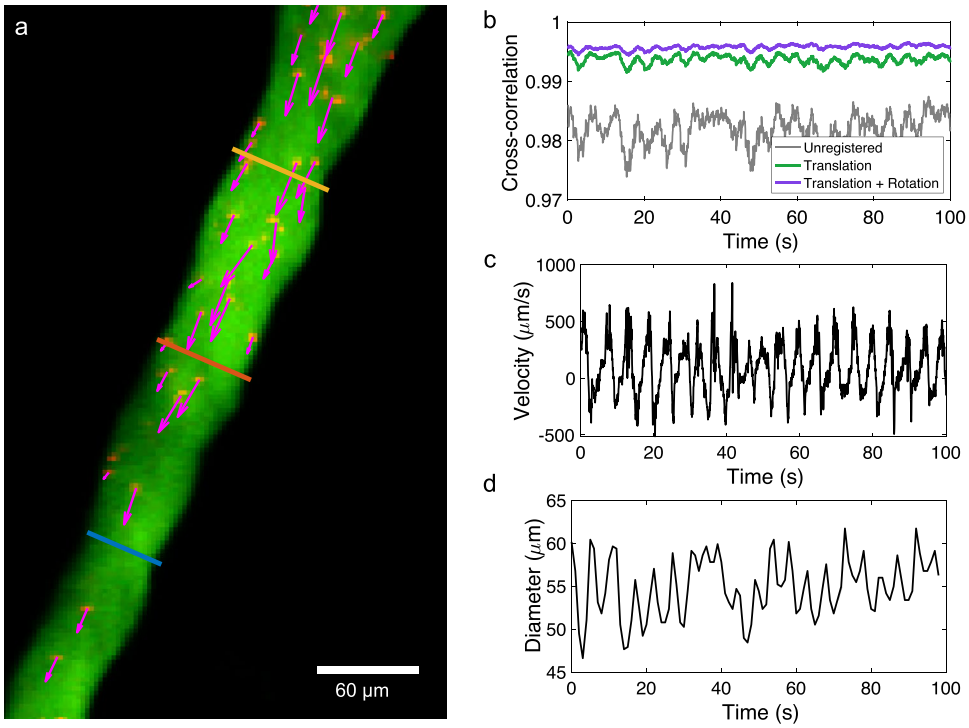


**Fig. 6** Image analysis techniques presented above, applied to a cervical lymphatic vessel. **a** TPM image of a cervical lymphatic vessel visualized using fluorescent dye (green) and microspheres (red). Magenta arrows represent instantaneous velocity of the particles inside the vessel. Three perpendicular colored lines indicate profile locations where the vessel diameter is measured. **b** A time series of normalized cross-correlation values with a moving average of 60 frames applied for three different cases: unregistered images (gray curve), images registered using rigid translation only (green curve), and images registered using both rigid translation and rotation (purple curve). **c** A time series of the spatially-averaged instantaneous velocity obtained from particle tracking. Positive value indicates prograde flow, while negative value indicates retrograde flow. **d** A time series of the instantaneous vessel diameter which reveals large amplitude contractions of the vessel that closely matches the timing of changes in fluid velocity plotted in (**c**)

Hussain et al. 2023, and Alzheimer's disease Ringstad et al. 2018). In this study, we outline image analysis techniques applied to images acquired from TPM which enable quantitative measurement of CSF flow at the surface of the brain. These scripts, as well as a short working example, are freely available online (Kim et al. 2023). Microspheres injected into the CSF are tracked via a predictive algorithm. These particle tracks can be superimposed to estimate the size and shape of PVSs, and velocity measurements can be binned in space and time-averaged to obtain a reliable estimate of the net flow speed. However, generating high-quality PTV requires image preprocessing. To account for minor shifts in the field of view that can result in erroneous CSF flow quantification, we performed registration via rigid translation using spatial cross-correlation on a time series of images. We highlighted a unique challenge that is encountered in this experimental protocol: Some microspheres may become stuck to the boundaries of PVSs, causing erroneous zero-velocity measurements. To solve this problem, we introduced three different masking methods and reported that dynamic masking is the most promising strategy. We also offered some tips for optimizing PTV parameters including threshold, minimum area, and maximum displacement. We demonstrated that near-optimal parameter values are typically identified iteratively with the criteria of maximizing the mean track length. Furthermore, we demonstrated how changes in vessel diameter, hypothesized to be an important driving mechanism of CSF flow, and can be measured in TPM images by identifying the location of the largest pixel intensity gradient to define the edges of the vessel and measure the diameter in time. Finally, we explored how the same image analysis techniques can be applied to cervical lymphatic vessels, which multiple studies indicate is an important route for CSF drainage (Bradbury and Cole 1980; Arnold et al. 1973; Ma et al. 2017; Hussain et al. 2023).

Our image analysis techniques for quantifying CSF dynamics offer a significant advantage in their automated tracking feature, whether for particle tracking or vessel diameter measurement. Some previous pioneering efforts have quantified CSF or lymph fluid flow through manual tracking of particles/cells (Bedussi et al. 2018; Dixon et al. 2005) and vessel edges across frames (Dixon et al. 2005). Such approaches are time consuming and prone to errors from operators. Our algorithm overcomes these limitations,

allowing for efficient and reliable analysis of tens of thousands of frames or more, leading to accurate measurements of velocity fields and vessel diameters (Mestre et al. 2018). Such measurements have enabled the first-ever estimates of key fluid mechanical parameters including the Reynolds number *Re*, Womersley number *Wo*, and volume flow rate *Q*. For a pial PVS $Re \approx 1 \times 10^{-3}$ (Mestre et al. 2018), $Wo \approx 0.1$ (Tithof et al. 2019), and $Q \approx 3 \times 10^{-3}$ µl/min (Mestre et al. 2018), while for a superficial cervical lymphatic vessel $Re \approx 8 \times 10^{-3}$, $Wo \approx 5 \times 10^{-2}$, and $Q \approx 2 \times 10^{-2}$ µl/min (Hussain et al. 2023).

The image analysis techniques presented here offer various advantages over other measurement modalities, largely owing to the capabilities of TPM. In particular, TPM stands out by its ability to generate high-resolution images (e.g., $512 \times 512$ dimensions with 0.5 µm/pixel) while maintaining an excellent frame rate (in excess of 30 Hz) at a precise imaging depth of up to several hundred micrometers into opaque tissue. These features are valuable when monitoring the flow of microspheres within the CSF and tracking vessel wall dynamics. We highlight that application of these techniques extends beyond the brain and cervical lymphatic vessels; these tools could be utilized to quantify flow in peripheral lymphatic vessels, assess CSF circulation in the spine, analyze blood flow within the cardiovascular system, or quantify a wide range of other biological processes.

The image analysis techniques discussed here utilize 2D imaging within a precise plane, estimated to have a depth of approximately 1 µm. It is important to note that this imaging plane is typically *not* perfectly aligned with the axis of the artery/lymphatic vessel, which is parallel to the direction of the net flow. Consequently, our measurements capture a 2D projection of a 3D flow, and the 3D flow can likely be accurately estimated from purely geometric considerations if the relative angle of the imaging plane and vessel axis is known. This could be achieved by reconstructing the 3D volume from a series of TPM 2D planes recorded at sequential depths (i.e., a TPM "z-stack"). Unfortunately, this approach greatly reduces the frame rate, making it unsuitable for 3D PTV applications. To achieve more precise measurements, fast 3D rastering TPM techniques are needed. Holographic PIV constitutes one potential approach that may enable 3D velocity measurements (Katz and Sheng 2010), as this technology has seen drastic improvements in recent years and increasing application to biological systems (You et al. 2020, 2018). However, holographic PIV has not been combined with TPM to the best of our knowledge, and doing so would likely constitute a tremendous technical challenge.

Many recent and ongoing studies aim to investigate the mechanisms by which CSF flow through PVSs is enhanced during sleep (Xie et al. 2013; Bojarskaite et al. 2023). The methodology presented here has previously been applied to mice that are anesthetized—not sleeping naturally (Mestre et al. 2018, 2020; Du et al. 2021; Raghunandan et al. 2021). Recent studies indicate that CSF flow varies substantially across different types of anesthesia (Hablitz et al. 2019) and in comparison with natural sleep (Benveniste et al. 2019). Training mice to fall asleep under a TPM is quite challenging but possible (Bojarskaite et al. 2023). A promising alternative approach to more easily image CSF dynamics under natural sleep may utilize a portable miniaturized TPM (Piyawattanametha et al. 2009; Ozbay et al. 2018). By attaching the portable TPM, CSF flow could be measured during normal behaviors, including natural sleep.

In this article, we have presented techniques for PTV applied in vivo in mice to quantify CSF dynamics. Such techniques have been used previously to characterize changes in CSF flow in acute arterial hypertension (Mestre et al. 2018) and neurovascular coupling (Holstein-Rønsbo et al. 2023), as well as following stroke (Mestre et al. 2020), cardiac arrest (Du et al. 2023), and traumatic brain injury (Hussain et al. 2023). These direct, quantitative measurements provide both parameterization (e.g., PVS size and Reynolds number) and validation (e.g., flow speed) which can be used to improve analytical/numerical models (Wang and Olbricht 2011; Mestre et al. 2020; Carr et al. 2021; Tithof et al. 2022; Boster et al. 2022). Future measurements may help quantify flow in different compartments to help settle open questions related to CSF/ISF transport (including IPAD, glymphatic, and other hypotheses). We emphasize that the techniques outlined here enable robust and efficient in vivo measurements. Such an in vivo approach is more reliable than inferring transport rates from ex vivo analysis of fixed tissue since recent studies (Mestre et al. 2018; Ma et al. 2019; Du et al. 2021) have revealed anatomical changes and irregular flows generated during the tissue fixation and/or death. However, despite consistent experimental protocols, the number of microspheres that appear in PVSs/cervical lymphatic vessels is quite variable for reasons that are not well-understood; future studies could vary microsphere injection protocols to optimize particle delivery to the imaging field and improve reliability of particle tracking. Measurement techniques outlined here may also prove valuable if applied to animals beyond mice, such as pigs, whose brains are gyrencephalic (i.e., have cortical folds, like the human brain) (Bèchet et al. 2021; Shanbhag et al. 2021). Finally, in vivo PTV may help in building a mechanistic understanding of how neuromodulation enhances glymphatic flow (Cheng et al. 2020; Choi et al. 2022; Min et al. 2023), perhaps facilitating the development of future medical devices and pharmaceutical approaches aimed at reducing the cognitive decline associated with a wide array of neurological conditions.

## Appendix A Particle tracking uncertainty analysis

In this Appendix, we analytically calculate the approximate uncertainty in particle tracking velocity measurements using propagation of error based on estimated uncertainties in particle position and image acquisition time. The numbers used here are specific for one particular data set (Kim et al. 2023), serving as a concrete example, but the reader could readily repeat these calculations for different imaging parameters. This derivation applies to two-photon microscopy, wherein each 2D image is assembled over a finite window in time during which each pixel is individually rastered. Hence, for images acquired at 29.6 Hz, each acquired image has an uncertainty of approximately $\Delta t = 33.8$ ms. Note this value is an upper bound for the temporal uncertainty, this upper bound will generally be larger/smaller when a greater/lesser number of pixels are recorded, and more precise (smaller) values of $\Delta t$ could be obtained by accounting for details of the TPM rastering technique.

The velocity of a tracked particle in frame $n$ can be estimated, to the first order, as $U_n = \frac{\Delta x}{\Delta t}$, where $\Delta x$ is the measured displacement of the particle since frame $n-1$, and $\Delta t$ is the measured time elapsed since frame $n-1$. Denoting the error in $\Delta x$ as $u_x$ and the error in $\Delta t$ as $u_t$, the error in $U_n$ is

$$\begin{aligned}\epsilon_U &= \left(\left(u_t\frac{\partial U_n}{\partial \Delta t}\right)^2 + \left(u_x\frac{\partial U_n}{\partial \Delta x}\right)^2\right)^{1/2} \\ &= \left(\left(u_t\frac{\Delta x}{\Delta t^2}\right)^2 + \left(u_x\frac{1}{\Delta t}\right)^2\right)^{1/2}.\end{aligned} \tag{A1}$$

Our image processing algorithm locates each particle by finding the centroid of a contiguous bright region above a given threshold, typically achieving error on the order of 0.1 pixel. In these data, each pixel has lateral dimension 1.04 µm, so we estimate $u_x \approx 0.104$ µm. As mentioned above, for a frame rate of 29.6 Hz, $\Delta t = 33.8$ ms. Now suppose the root-mean-square single-frame displacement is $\Delta x = 2.158$ µm (this value is obtained empirically by performing particle tracking). Estimating the timing error $u_t$ for a two-photon microscope is subtle because images are produced not by making simultaneous measurements from an array of sensors but by making subsequent measurements as the single focal point rasters the field of view. If the focal point traces column-by-column, then measuring a particle moving to an adjacent column involves greater timing error than measuring a particle moving to an adjacent row. Considering image dimensions $512 \times 512$ pixels, the two timing errors would be roughly $\Delta t/512$ and $\Delta t/512^2$, respectively. To be conservative, we take $u_t \approx \Delta t/512 = 66.0$ µs. Using these values, we find $\epsilon_U = 3.08$ µm/s.

In practice, we estimate the velocity with a higher-order method, convolving the measured position with a kernel that provides differentiation and smoothing. Explicitly, the numerical scheme used in our code makes the estimate

$$U_n = \frac{\alpha\Delta\widetilde{x}}{\Delta t}, \tag{A2}$$

where $\alpha = 2/(\pi^{1/2}\mathrm{erf}(3) - 6e^{-9}) \approx 1.129$ and

$$\begin{aligned}\Delta\widetilde{x} = &-3e^{-9}x_{n-3} - 2e^{-4}x_{n-2} - e^{-1}x_{n-1} + e^{1}x_{n+1} \\ &+ 2e^{-4}x_{n+2} + 3e^{-9}x_{n+3}.\end{aligned} \tag{A3}$$

The velocity error is

$$\begin{aligned}\epsilon_U = &\left(\left(u_t\frac{\partial U_n}{\partial \Delta t}\right)^2 + \left(u_{n-3}\frac{\partial U_n}{\partial x_{n-3}}\right)^2 + \left(u_{n-2}\frac{\partial U_n}{\partial x_{n-2}}\right)^2 \cdots \right. \\ &\left. + \left(u_{n-1}\frac{\partial U_n}{\partial x_{n-1}}\right)^2 + \left(u_{n+1}\frac{\partial U_n}{\partial x_{n+1}}\right)^2 + \left(u_{n+2}\frac{\partial U_n}{\partial x_{n+2}}\right)^2 + \left(u_{n+3}\frac{\partial U_n}{\partial x_{n+3}}\right)^2\right)^{1/2},\end{aligned} \tag{A4}$$

where $u_{n-3}$ is the measurement error associated with location $x_{n-3}$, $u_{n-2}$ is the measurement error associated with location $x_{n-2}$, and so on. Assuming homogeneity implies that all those errors have the same value, which we again denote $u_x$. Then, the velocity error becomes

$$\epsilon_U = \alpha\left(\left(u_t\frac{\Delta\widetilde{x}}{\Delta t^2}\right)^2 + \beta\left(u_x\frac{1}{\Delta t}\right)^2\right)^{1/2}, \tag{A5}$$

where $\beta = 18e^{-18} + 8e^{-8} + 2e^{-2} \approx 0.273$. To estimate the value of $\Delta\widetilde{x}$, we consider the case in which a particle's displacement between any two frames is the measured root-mean-square value $\Delta x$, implying $x_{n+1} - x_{n-1} = 2\Delta x$, $x_{n+2} - x_{n-2} = 4\Delta x$, and $x_{n+3} - x_{n-3} = 6\Delta x$. Therefore, $\Delta\widetilde{x} = \gamma^{1/2}\Delta x$, where $\gamma = (2e^{-1} + 8e^{-4} + 18e^{-9})^2 \approx 0.782$. Altogether, the velocity error is

$$\epsilon_U = \alpha\left(\gamma\left(u_t\frac{\Delta x}{\Delta t^2}\right)^2 + \beta\left(u_x\frac{1}{\Delta t}\right)^2\right)^{1/2}. \tag{A6}$$

Comparing to Eq. (A1), we see that the error in velocity estimated with the higher-order numerical scheme differs from the error in the first-order velocity estimates only by factors of order unity. Again taking the same values for $u_t$, $u_x$, $\Delta t$, and $\Delta x$, the velocity error in the higher-order scheme is $\epsilon_U = 1.82$ µm/s, about 40% lower than with the first-order estimate.

**Acknowledgements** We thank Kim Boster for valuable insight and suggestions, as well as substantial contributions to the development of our MATLAB visualization tool "imagei.m." We also thank Keelin Quirk for implementing more advanced kinematic predictions in our particle tracking MATLAB script "PredictiveTracker.m."

**Author Contributions** JT, DHK, and MN helped in conceptualization; JT and DHK helped in methodology; DK and YG helped in formal

analysis and investigation; DK, JT, and DHK contributed to writing—original draft preparation; JT and DHK contributed to writing—review and editing; JT, DHK, and MN worked in funding acquisition; JT, DHK, and MN worked in resources; and JT, DHK, and MN worked in supervision.

**Funding** DK and JT are supported by a Career Award at the Scientific Interface from Burroughs Wellcome Fund. YG, MN, and DHK are supported by NIH BRAIN Initiative U19NS128613, NIH National Center for Complementary and Integrative Health R01AT012312, and US Army MURI W911NF1910280.

**Data Availability** A short working example including two-photon images and MATLAB scripts is available at https://doi.org/10.5281/zenodo.8165799.

## Declarations

**Conflict of Interest** The authors have no competing interests to declare that are relevant to the content of this article.

**Ethical Approval** Animal experiments were approved by the Danish Animal Experiments Inspectorate or the University Committee on Animal Resources of the University of Rochester and performed according to guidelines from the National Institutes of Health (NIH).

## References

Abbott NJ (2004) Evidence for bulk flow of brain interstitial fluid: significance for physiology and pathology. Neurochem Int 45(4):545–552

Abbott NJ, Pizzo ME, Preston JE, Janigro D, Thorne RG (2018) The role of brain barriers in fluid movement in the CNS: is there a 'glymphatic' system? Acta Neuropathol 135(3):387–407

Agarwal N, Carare RO (2021) Cerebral vessels: an overview of anatomy, physiology, and role in the drainage of fluids and solutes. Front Neurol 11:1748

Ahn JH, Cho H, Kim J-H, Kim SH, Ham J-S, Park I, Suh SH, Hong SP, Song J-H, Hong Y-K, Jeong Y, Park S-H, Koh GY (2019) Meningeal lymphatic vessels at the skull base drain cerebrospinal fluid. Nature 572(7767):62–66. https://doi.org/10.1038/s41586-019-1419-5

Albargothy NJ, Johnston DA, MacGregor-Sharp M, Weller RO, Verma A, Hawkes CA, Carare RO (2018) Convective influx/glymphatic system: tracers injected into the CSF enter and leave the brain along separate periarterial basement membrane pathways. Acta Neuropathol 136(1):139–152

Aldea R, Weller RO, Wilcock DM, Carare RO, Richardson G (2019) Cerebrovascular smooth muscle cells as the drivers of intramural periarterial drainage of the brain. Front Aging Neurosci 11:1

Arnold W, Ritter R, Wagner W (1973) Quantitative studies on the drainage of the cerebrospinal fluid into the lymphatic system. Acta Oto-Laryngol 76(1–6):156–161

Asgari M, Zélicourt D, Kurtcuoglu V (2016) Glymphatic solute transport does not require bulk flow. Sci Rep 6(1):38635

Aspelund A, Antila S, Proulx ST, Karlsen TV, Karaman S, Detmar M, Wiig H, Alitalo K (2015) A dural lymphatic vascular system that drains brain interstitial fluid and macromolecules. J Exp Med 212(7):991–999

Battal B, Kocaoglu M, Bulakbasi N, Husmen G, Tuba Sanal H, Tayfun C (2011) Cerebrospinal fluid flow imaging by using phase-contrast MR technique. Brit J Radiol 84(1004):758–765

Bedussi B, Almasian M, Vos J, VanBavel E, Bakker EN (2018) Paravascular spaces at the brain surface: Low resistance pathways for cerebrospinal fluid flow. J Cerebr Blood F Met 38(4):719–726

Benveniste H, Liu X, Koundal S, Sanggaard S, Lee H, Wardlaw J (2019) The glymphatic system and waste clearance with brain aging: a review. Gerontology 65(2):106–119

Bohr T, Hjorth PG, Holst SC, Hrabětová S, Kiviniemi V, Lilius T, Lundgaard I, Mardal K-A, Martens EA, Mori Y, Nägerl UV, Nicholson C, Tannenbaum A, Thomas JH, Tithof J, Benveniste H, Iliff JJ, Kelley DH, Nedergaard M (2022) The glymphatic system: Current understanding and modeling. iScience 25(9):104987. https://doi.org/10.1016/j.isci.2022.104987

Bojarskaite L, Vallet A, Bjørnstad DM, Gullestad Binder KM, Cunen C, Heuser K, Kuchta M, Mardal K-A, Enger R (2023) Sleep cycle-dependent vascular dynamics in male mice and the predicted effects on perivascular cerebrospinal fluid flow and solute transport. Nat Commun 14(1):953

Boster KAS, Tithof J, Cook DD, Thomas JH, Kelley DH (2022) Sensitivity analysis on a network model of glymphatic flow. J Roy Soc Interface. https://doi.org/10.1098/rsif.2022.0257

Bradbury M, Cole D (1980) The role of the lymphatic system in drainage of cerebrospinal fluid and aqueous humour. J Physiol 299(1):353–365

Bradley W (2015) CSF flow in the brain in the context of normal pressure hydrocephalus. Am J Neuroradiol 36(5):831–838

Bèchet NB, Shanbhag NC, Lundgaard I (2021) Glymphatic pathways in the gyrencephalic brain. J Cerebr Blood F Met 41(9):2264–2279

Carare R, Bernardes-Silva M, Newman T, Page A, Nicoll J, Perry V, Weller R (2008) Solutes, but not cells, drain from the brain parenchyma along basement membranes of capillaries and arteries: significance for cerebral amyloid angiopathy and neuroimmunology. Neuropath Appl Neuro 34(2):131–144

Carr JB, Thomas JH, Liu J, Shang JK (2021) Peristaltic pumping in thin non-axisymmetric annular tubes. J Fluid Mech. https://doi.org/10.1017/jfm.2021.277

Charogiannis A, An JS, Markides CN (2015) A simultaneous planar laser-induced fluorescence, particle image velocimetry and particle tracking velocimetry technique for the investigation of thin liquid-film flows. Exp Therm Fluid Sci 68:516–536

Cheng KP, Brodnick SK, Blanz SL, Zeng W, Kegel J, Pisaniello JA, Ness JP, Ross E, Nicolai EN, Settell ML et al (2020) Clinically-derived vagus nerve stimulation enhances cerebrospinal fluid penetrance. Brain Stimul 13(4):1024–1030. https://doi.org/10.1016/j.brs.2020.03.012

Choi S, Jang DC, Chung G, Kim SK (2022) Transcutaneous auricular vagus nerve stimulation enhances cerebrospinal fluid circulation and restores cognitive function in the rodent model of vascular cognitive impairment. Cells 11(19):3019

Croci M, Vinje V, Rognes ME (2019) Uncertainty quantification of parenchymal tracer distribution using random diffusion and convective velocity fields. Fluids Barriers CNS 16(1):1–21

Cserr HF, Cooper DN, Suri PK, Patlak CS (1981) Efflux of radiolabeled polyethylene glycols and albumin from rat brain. Am J Physiol–Renal 240(4):319–328

Cserr HF, Ostrach L (1974) Bulk flow of interstitial fluid after intracranial injection of blue dextran 2000. Exp Neurol 45(1):50–60

Decker Y, Krämer J, Xin L, Müller A, Scheller A, Fassbender K, Proulx ST (2022) Magnetic resonance imaging of cerebrospinal fluid outflow after low-rate lateral ventricle infusion in mice. JCI Insight 7(3):e150881

Diem AK, MacGregor Sharp M, Gatherer M, Bressloff NW, Carare RO, Richardson G (2017) Arterial pulsations cannot drive

intramural periarterial drainage: significance for a $\beta$ drainage. Front Neurosci 11:475
Diezmann L, Shechtman Y, Moerner W (2017) Three-dimensional localization of single molecules for super-resolution imaging and single-particle tracking. Chem Rev 117(11):7244–7275
Dixon JB, Zawieja DC, Gashev AA, Coté GL (2005) Measuring microlymphatic flow using fast video microscopy. J Biomed Opt 10(6):064016–064016
Du T, Mestre H, Kress BT, Liu G, Sweeney AM, Samson AJ, Rasmussen MK, Mortensen KN, Bork PAR, Peng W, Olveda GE, Bashford L, Toro ER, Tithof J, Kelley DH, Thomas JH, Hjorth PG, Martens EA, Mehta RI, Hirase H, Mori Y, Nedergaard M (2021) Cerebrospinal fluid is a significant fluid source for anoxic cerebral oedema. Brain 145(2):787–797. https://doi.org/10.1093/brain/awab293
Du T, Raghunandan A, Mestre H, Plá V, Liu G, Ladrón-de-Guevara A, Nedergaard M, Kelley DH (2023). Restoration of cervical lymphatic vessel function in aging rescues cerebrospinal fluid drainage. Submitted
Eide PK, Vatnehol SAS, Emblem KE, Ringstad G (2018) Magnetic resonance imaging provides evidence of glymphatic drainage from human brain to cervical lymph nodes. Sci Rep. https://doi.org/10.1038/s41598-018-25666-4
Ergin FG (2017) Dynamic masking techniques for particle image velocimetry. Isi Bilim Tek Der 37(2):61–74
Ergin FG (2017) Dynamic masking techniques for particle image velocimetry. Isi Bilim Tek Derg 37(2):61–74
Faghih MM, Sharp MK (2021) Mechanisms of tracer transport in cerebral perivascular spaces. J Biomech 118:110278
Gülan U, Lüthi B, Holzner M, Liberzon A, Tsinober A, Kinzelbach W (2012) Experimental study of aortic flow in the ascending aorta via particle tracking velocimetry. Exp Fluids 53:1469–1485
Hablitz LM, Nedergaard M (2021) The glymphatic system. Curr Biol 31(20):1371–1375. https://doi.org/10.1016/j.cub.2021.08.026
Hablitz LM, Plá V, Giannetto M, Vinitsky HS, Stæger FF, Metcalfe T, Nguyen R, Benrais A, Nedergaard M (2020) Circadian control of brain glymphatic and lymphatic fluid flow. Nat Commun 11(1):4411
Hablitz LM, Vinitsky HS, Sun Q, Stæger FF, Sigurdsson B, Mortensen KN, Lilius TO, Nedergaard M (2019) Increased glymphatic influx is correlated with high EEG delta power and low heart rate in mice under anesthesia. Science Adv 5(2):5447
Hadaczek P et al (2006) The "perivascular pump'' driven by arterial pulsation is a powerful mechanism for the distribution of therapeutic molecules within the brain. Mol Ther 14(1):69–78
Hand A, Sun T, Barber D, Hose D, MacNeil S (2009) Automated tracking of migrating cells in phase-contrast video microscopy sequences using image registration. J Microsc 234(1):62–79
Hill DL, Batchelor PG, Holden M, Hawkes DJ (2001) Medical image registration. Phys Med Biol 46(3):1
Hilsenbeck O, Schwarzfischer M, Skylaki S, Schauberger B, Hoppe PS, Loeffler D, Kokkaliaris KD, Hastreiter S, Skylaki E, Filipczyk A et al (2016) Software tools for single-cell tracking and quantification of cellular and molecular properties. Nat Biotechnol 34(7):703–706
Hladky SB, Barrand MA (2022) The glymphatic hypothesis: the theory and the evidence. Fluids Barriers CNS 19(1):1–33
Holstein-Rønsbo S, Gan Y, Giannetto MJ, Rasmussen MK, Sigurdsson B, Beinlich FRM, Rose L, Untiet V, Hablitz LM, Kelley DH, Nedergaard M (2023) Glymphatic influx and clearance are accelerated by neurovascular coupling. Nat Neurosci 26:1042–1053
Hussain R, Tithof J, Wang W, Cheetham-West A, Song W, Peng W, Kim D, Sun Q, Peng S, Plá V, Kelley DH, Hirase H, Castorena-Gonzalez JA, Weikop P, Goldman SA, Davis MJ, Nedergaard M (2023). Potentiating glymphatic drainage minimizes post-traumatic cerebral edema. Submitted
Iliff JJ, Wang M, Liao Y, Plogg BA, Peng W, Gundersen GA, Benveniste H, Vates GE, Deane R, Goldman SA, Nagelhus EA, Nedergaard M (2012) A paravascular pathway facilitates CSF flow through the brain parenchyma and the clearance of interstitial solutes, including amyloid β. Sci Transl Med 4(147):111–147
Iliff JJ, Wang M, Zeppenfeld DM, Venkataraman A, Plog BA, Liao Y et al (2013) Cerebral arterial pulsation drives paravascular CSF-interstitial fluid exchange in the murine brain. J Neurosci 33(46):18190–18199
Jessen NA, Munk ASF, Lundgaard I, Nedergaard M (2015) The glymphatic system: a beginner's guide. Neurochem Res 40(12):2583–2599
Jonas S, Bhattacharya D, Khokha MK, Choma MA (2011) Microfluidic characterization of cilia-driven fluid flow using optical coherence tomography-based particle tracking velocimetry. Biomed Opt Express 2(7):2022–2034
Katz J, Sheng J (2010) Applications of holography in fluid mechanics and particle dynamics. Annu Rev Fluid Mech 42:531–555
Kelley DH, Ouellette NT (2011) Using particle tracking to measure flow instabilities in an undergraduate laboratory experiment. Am J Phys 79(3):267–273
Kelley DH, Thomas JH (2022) Cerebrospinal fluid flow. Annu Rev Fluid Mech. https://doi.org/10.1146/annurev-fluid-120720-011638
Kim D, Gan Y, Nedergaard M, Kelley DH, Tithof J (2023) Image Analysis Techniques for In Vivo Quantification of Cerebrospinal Fluid Flow. Zenodo. https://doi.org/10.5281/zenodo.8165799
Kiviniemi V, Wang X, Korhonen V, Keinänen T, Tuovinen T, Autio J, LeVan P, Keilholz S, Zang Y-F, Hennig J, Nedergaard M (2015) Ultra-fast magnetic resonance encephalography of physiological brain activity - glymphatic pulsation mechanisms? J Cereb Blood Flow Met 36(6):1033–1045. https://doi.org/10.1177/0271678x15622047
Li Y, Amili O, Coletti F (2022) Experimental study of concentrated particle transport in successively bifurcating vessels. Phys Rev Fluids 7(8):083101
Li G, Cao Y, Tang X, Huang J, Cai L, Zhou L (2022) The meningeal lymphatic vessels and the glymphatic system: Potential therapeutic targets in neurological disorders. J Cerebr Blood F Met 42(8):1364–1382
Louveau A, Smirnov I, Keyes TJ, Eccles JD, Rouhani SJ, Peske JD, Derecki NC, Castle D, Mandell JW, Lee KS et al (2015) Structural and functional features of central nervous system lymphatic vessels. Nature 523(7560):337–341
Louveau A, Smirnov I, Keyes TJ, Eccles JD, Rouhani SJ, Peske JD, Derecki NC, Castle D, Mandell JW, Lee KS, Harris TH, Kipnis J (2016) Structural and functional features of central nervous system lymphatic vessels. Nature 533(7602):278–278. https://doi.org/10.1038/nature16999
Ma Q, Ineichen BV, Detmar M, Proulx ST (2017) Outflow of cerebrospinal fluid is predominantly through lymphatic vessels and is reduced in aged mice. Nat Commun 8(1):1434
Ma Q, Ries M, Decker Y, Müller A, Riner C, Bücker A et al (2019) Rapid lymphatic efflux limits cerebrospinal fluid flow to the brain. Acta Neuropathol 137(1):151–165
Manzo C, Garcia-Parajo MF (2015) A review of progress in single particle tracking: from methods to biophysical insights. Rep Prog Phys 78(12):124601
Mesquita SD, Louveau A, Vaccari A, Smirnov I, Cornelison RC, Kingsmore KM, Contarino C, Onengut-Gumuscu S, Farber E, Raper D, Viar KE, Powell RD, Baker W, Dabhi N, Bai R, Cao R, Hu S, Rich SS, Munson JM, Lopes MB, Overall CC, Acton ST, Kipnis J (2018) Functional aspects of meningeal lymphatics in ageing and Alzheimer's disease. Nature 560(7717):185–191. https://doi.org/10.1038/s41586-018-0368-8
...Mestre H, Du T, Sweeney AM, Liu G, Samson AJ, Peng W, Mortensen KN, Stæger FF, Bork PAR, Bashford L, Toro ER,

Tithof J, Kelley DH, Thomas JH, Hjorth PG, Martens EA, Mehta RI, Solis O, Blinder P, Kleinfeld D, Hirase H, Mori Y, Nedergaard M (2020) Cerebrospinal fluid influx drives acute ischemic tissue swelling. Science 367(6483):eaax7171

Mestre H, Kostrikov S, Mehta RI, Nedergaard M (2017) Perivascular spaces, glymphatic dysfunction, and small vessel disease. Clin Sci 131(17):2257–2274

Mestre H, Tithof J, Du T, Song W, Peng W, Sweeney AM, Olveda G, Thomas JH, Nedergaard M, Kelley DH (2018) Flow of cerebrospinal fluid is driven by arterial pulsations and is reduced in hypertension. Nat Commun 9(1):4878

Milhorat TH (1975) The third circulation revisited. J Neurosurg 42(6):628–645

Min J, Rouanet J, Martini AC, Nashiro K, Yoo HJ, Porat S, Cho C, Wan J, Cole SW, Head E et al (2023) Modulating heart rate oscillation affects plasma amyloid beta and tau levels in younger and older adults. Sci Rep 13(1):3967

Moore JE Jr, Bertram CD (2018) Lymphatic system flows. Annu Rev Fluid Mech 50:459–482

Murtha LA, Yang Q, Parsons MW, Levi CR, Beard DJ, Spratt NJ, McLeod DD (2014) Cerebrospinal fluid is drained primarily via the spinal canal and olfactory route in young and aged spontaneously hypertensive rats. Fluids Barriers CNS 11(1):1–9

Møllgård K, Beinlich FR, Kusk P, Miyakoshi LM, Delle C, Plá V, Hauglund NL, Esmail T, Rasmussen MK, Gomolka RS et al (2023) A mesothelium divides the subarachnoid space into functional compartments. Science 379(6627):84–88

Møllgård K, Beinlich FR, Kusk P, Miyakoshi LM, Delle C, Plá V, Hauglund NL, Esmail T, Rasmussen MK, Gomolka RS et al (2023) A mesothelium divides the subarachnoid space into functional compartments. Science 379(6627):84–88

Nedergaard M, Goldman SA (2020) Glymphatic failure as a final common pathway to dementia. Science 370(6512):50–56

Norwood JN, Zhang Q, Card D, Craine A, Ryan TM, Drew PJ (2019) Anatomical basis and physiological role of cerebrospinal fluid transport through the murine cribriform plate. eLife 8:44278

Ouellette NT, Xu H, Bodenschatz E (2006) A quantitative study of three-dimensional lagrangian particle tracking algorithms. Exp Fluids 40:301–313

Ozbay BN, Futia GL, Ma M, Bright VM, Gopinath JT, Hughes EG, Restrepo D, Gibson EA (2018) Three dimensional two-photon brain imaging in freely moving mice using a miniature fiber coupled microscope with active axial-scanning. Sci Rep 8(1):8108

Piyawattanametha W, Cocker ED, Burns LD, Barretto RP, Jung JC, Ra H, Solgaard O, Schnitzer MJ (2009) In vivo brain imaging using a portable 2.9 g two-photon microscope based on a microelectromechanical systems scanning mirror. Opt Lett 34(15):2309–2311

Plog BA, Mestre H, Olveda GE, Sweeney AM, Kenney HM, Cove A, Dholakia KY, Tithof J, Nevins TD, Lundgaard I et al (2018) Transcranial optical imaging reveals a pathway for optimizing the delivery of immunotherapeutics to the brain. JCI Insight 3(20):e120922

Proulx ST (2021) Cerebrospinal fluid outflow: a review of the historical and contemporary evidence for arachnoid villi, perineural routes, and dural lymphatics. Cell Mol Life Sci 78(6):2429–2457

Raghunandan A, Ladron-de-Guevara A, Tithof J, Mestre H, Du T, Nedergaard M, Thomas JH, Kelley DH (2021) Bulk flow of cerebrospinal fluid observed in periarterial spaces is not an artifact of injection. eLife 10:65958

Ramos M, Burdon Bechet N, Battistella R, Pavan C, Xavier ALR, Nedergaard M, Lundgaard I (2019) Cisterna magna injection in rats to study glymphatic function 97–104

Rasmussen MK, Mestre H, Nedergaard M (2018) The glymphatic pathway in neurological disorders. Lancet Neurol 17(11):1016–1024

Rasmussen MK, Mestre H, Nedergaard M (2021) Fluid transport in the brain. Physiol Rev 102(2):1025–1151

Ray LA, Heys JJ (2019) Fluid flow and mass transport in brain tissue. Fluids 4(4):196

Rennels ML, Gregory TF, Blaumanis OR, Fujimoto K, Grady PA (1985) Evidence for a 'paravascular' fluid circulation in the mammalian central nervous system, provided by the rapid distribution of tracer protein throughout the brain from the subarachnoid space. Brain Res 326(1):47–63

Rey J, Sarntinoranont M (2018) Pulsatile flow drivers in brain parenchyma and perivascular spaces: a resistance network model study. Fluids Barriers CNS 15(1):20

Ringstad G, Valnes LM, Dale AM, Pripp AH, Vatnehol S-AS, Emblem KE, Mardal K-A, Eide PK (2018) Brain-wide glymphatic enhancement and clearance in humans assessed with MRI. JCI Insight 3(13):e121537

Salminen AT, Tithof J, Izhiman Y, Masters EA, McCloskey MC, Gaborski TR, Kelley DH, Pietropaoli AP, Waugh RE, McGrath JL (2020) Endothelial cell apicobasal polarity coordinates distinct responses to luminally versus abluminally delivered TNF-$\alpha$ in a microvascular mimetic. Integr Biol 12(11):275–289

Schley D, Carare-Nnadi R, Please CP, Perry VH, Weller RO (2006) Mechanisms to explain the reverse perivascular transport of solutes out of the brain. J Theor Biol 238(4):962–974

Sengupta PP, Pedrizetti G, Narula J (2012) Multiplanar visualization of blood flow using echocardiographic particle imaging velocimetry. JACC Cardiovasc Imag 5(5):566–569

Shanbhag NC, Bèchet NB, Kritsilis M, Lundgaard I (2021) Impaired cerebrospinal fluid transport due to idiopathic subdural hematoma in pig: an unusual case. BMC Vet Res 17:1–8

Smith AJ, Verkman AS (2018) The "glymphatic'' mechanism for solute clearance in Alzheimer's disease: game changer or unproven speculation? FASEB J 32(2):543–551

So PT, Dong CY, Masters BR, Berland KM (2000) Two-photon excitation fluorescence microscopy. Annu Rev Biomed Eng 2(1):399–429

Spector R, Snodgrass SR, Johanson CE (2015) A balanced view of the cerebrospinal fluid composition and functions: Focus on adult humans. Exp Neurol 273:57–68

Spera I, Cousin N, Ries M, Kedracka A, Castillo A, Aleandri S, Vladymyrov M, Mapunda JA, Engelhardt B, Luciani P, Detmar M, Proulx ST (2023) Open pathways for cerebrospinal fluid outflow at the cribriform plate along the olfactory nerves. EBioMedicine 91

Steffensen AB, Edelbo BL, Barbuskaite D, Andreassen SN, Olsen MH, Møller K, MacAulay N (2023) Nocturnal increase in cerebrospinal fluid secretion as a circadian regulator of intracranial pressure. Fluids Barriers CNS 20(1):1–14

Sweeney AM, Plá V, Du T, Liu G, Sun Q, Peng S, Plog BA, Kress BT, Wang X, Mestre H et al (2019) In vivo imaging of cerebrospinal fluid transport through the intact mouse skull using fluorescence macroscopy. JoVE-J Vis Exp 149:e59774

Tithof J, Kelley DH, Mestre H, Nedergaard M, Thomas JH (2019) Hydraulic resistance of periarterial spaces in the brain. Fluids Barriers CNS 16(19):1–13

Tithof J, Boster KAS, Bork PAR, Nedergaard M, Thomas JH, Kelley DH (2022) A network model of glymphatic flow under different experimentally-motivated parametric scenarios. iScience

Vennemann P, Lindken R, Westerweel J (2007) In vivo whole-field blood velocity measurement techniques. Exp Fluids 42:495–511

Vindedal GF, Thoren AE, Jensen V, Klungland A, Zhang Y, Holtzman MJ, Ottersen OP, Nagelhus EA (2016) Removal of aquaporin-4 from glial and ependymal membranes causes brain water accumulation. Mol Cell Neurosci 77:47–52

Vinje V, Eklund A, Mardal K-A, Rognes ME, Støverud K-H (2020) Intracranial pressure elevation alters csf clearance pathways. Fluids Barriers CNS 17(1):1–19

Wang H, Li Z, Zhang X, Zhu L, Liu Y, Wang S (2020) The motion of respiratory droplets produced by coughing. Phys Fluids 32(12):125102

Wang P, Olbricht WL (2011) Fluid mechanics in the perivascular space. J Theor Biol 274(1):52–57

Weller RO (1998) Pathology of cerebrospinal fluid and interstitial fluid of the CNS: significance for Alzheimer disease, prion disorders and multiple sclerosis. J Neuropath Exp Neur 57(10):885–894

Wright BL, Lai JT, Sinclair AJ (2012) Cerebrospinal fluid and lumbar puncture: a practical review. J Neurol 259(8):1530–1545

Xavier AL, Hauglund NL, Holstein-Rathlou S, Li Q, Sanggaard S, Lou N, Lundgaard I, Nedergaard M (2018) Cannula implantation into the cisterna magna of rodents. JoVE-J Vis Exp 135:57378

Xie L, Kang H, Xu Q, Chen MJ, Liao Y, Thiyagarajan M, O'Donnell J, Christensen DJ, Nicholson C, Iliff JJ, Takano T, Deane R, Nedergaard M (2013) Sleep drives metabolite clearance from the adult brain. Science 342(6156):373–377

Yamada M (2015) Cerebral amyloid angiopathy: emerging concepts. J Stroke 17(1):17

Yardeni T, Eckhaus M, Morris HD, Huizing M, Hoogstraten-Miller S (2011) Retro-orbital injections in mice. Lab Animal 40(5):155–160

You J, Mallery K, Hong J, Hondzo M (2018) Temperature effects on growth and buoyancy of microcystis aeruginosa. J Plankton Res 40(1):16–28

You J, Mallery K, Mashek DG, Sanders M, Hong J, Hondzo M (2020) Microalgal swimming signatures and neutral lipids production across growth phases. Biotechnol Bioeng 117(4):970–980